Blood–brain barrier opening by intracarotid artery hyperosmolar mannitol induces sterile inflammatory and innate immune responses

Scott R. Burks[a,1,2], Cymon N. Kersch[b,1], Jaclyn A. Witko[a], Michael A. Pagel[b], Maggie Sundby[a], Leslie L. Muldoon[b], Edward A. Neuwelt[b,c,d], and Joseph A. Frank[a,e,2]

[a]Frank Laboratory, Radiology and Imaging Sciences, NIH Clinical Center, Bethesda, MD 20895; [b]Department of Neurology, Oregon Health & Science University, Portland, OR 97239; [c]Department of Neurological Surgery, Oregon Health & Science University, Portland, OR 97239; [d]Portland Veterans Affairs Medical Center, Portland, OR 97239; and [e]National Institute of Biomedical Imaging and Bioengineering, Bethesda, MD 20895

Edited by David M. Holtzman, Washington University School of Medicine, St. Louis, MO, and accepted by Editorial Board Member Philippa Marrack March 22, 2021 (received for review November 16, 2020)

Intracarotid arterial hyperosmolar mannitol (ICAHM) blood–brain barrier disruption (BBBD) is effective and safe for delivery of therapeutics for central nervous system malignancies. ICAHM osmotically alters endothelial cells and tight junction integrity to achieve BBBD. However, occurrence of neuroinflammation following hemispheric BBBD by ICAHM remains unknown. Temporal proteomic changes in rat brains following ICAHM included increased damage-associated molecular patterns, cytokines, chemokines, trophic factors, and cell adhesion molecules, indicative of a sterile inflammatory response (SIR). Proteomic changes occurred within 5 min of ICAHM infusion and returned to baseline by 96 h. Transcriptomic analyses following ICAHM BBBD further supported an SIR. Immunohistochemistry revealed activated astrocytes, microglia, and macrophages. Moreover, proinflammatory proteins were elevated in serum, and proteomic and histological findings from the contralateral hemisphere demonstrated a less pronounced SIR, suggesting neuroinflammation beyond regions of ICAHM infusion. Collectively, these results demonstrate ICAHM induces a transient SIR that could potentially be harnessed for neuroimmunomodulation.

blood–brain barrier | hyperosmolar mannitol | sterile inflammation | neuroinflammation

The primary function of the blood–brain barrier (BBB) is to maintain brain homeostasis by limiting the transit of infectious agents, plasma proteins, toxins, drugs, and cells from systemic circulation into the parenchyma while simultaneously permitting oxygen and glucose transport to sustain brain metabolic functions (1–3). The BBB consists of specialized endothelial cells that are connected through various tight junction proteins (TJP) and bordered abluminally by a unique basement membrane and astrocyte endfeet. This specialized endothelial barrier is one part of the neurovascular unit (NVU), which includes pericytes, microglia, astrocytes, neurons, and extracellular matrix to coordinate cerebral vasculature function with neuronal activity (1, 3–8). Although the BBB critically protects the brain, it also inhibits central nervous system (CNS) delivery of therapeutic agents for neurological diseases and cancers. BBB integrity is inconsistent in central nervous system (CNS) malignancies, ranging from nearly impermeable to a completely ineffectual barrier (9). Heterogeneous NVU function within the tumor, the proliferating edge, and peritumoral brain results in low and inconsistent delivery of chemotherapy and other targeted therapeutics (10).

Various techniques have been used to cause transient BBBD and allow delivery of chemotherapeutic agents, antibodies, genes, and nanoparticles to treat CNS diseases and malignancies (11–20). These techniques include intracarotid artery infusion of hyperosmolar mannitol (ICAHM), convection-enhanced delivery, and magnetic resonance imaging (MRI)–guided pulsed focused ultrasound (pFUS) in combination with intravascular microbubbles (MB) (10, 11, 14, 15, 17, 19–26). Following BBBD, the cellular elements of the NVU respond to an influx of plasma protein with an increased expression of cell adhesion molecules (CAM) on the luminal surface and the transient release of damage-associated molecular patterns (DAMPs), cytokines, chemokines, and trophic factors (CCTF) from microglia, astrocytes, and endothelium (4, 21, 27–36). Increased CCTF and CAM in the absence of an infectious agent defines a sterile inflammatory response (SIR), which in turn can induce an influx of systemic mononuclear cells into the parenchyma (21, 28, 29, 31, 32).

Previous studies have shown that noninvasive MRI-guided pFUS+MB, which effectively causes BBBD in various preclinical experimental models and clinical trials, induces an SIR in the absence of cerebral damage (21, 24–26, 37–40). Within 5 min after pFUS+MB, increased interferon gamma (IFNγ) levels were observed, which can stimulate an innate immune response (41, 42). It has been hypothesized that the SIR stimulated by pFUS+MB–induced BBBD may have utility in treating neurological disorders. However, pFUS+MB has been limited in early clinical studies due to the relatively small brain volumes that can be disrupted (11, 12, 14, 15). Improvements in pFUS+MB technologies in combination

Significance

Disruption of the blood–brain barrier (BBB) for drug delivery to the central nervous system (CNS) is achieved clinically through intracarotid artery hyperosmotic mannitol (ICAHM) infusions. However, ICAHM is often viewed as a simple drug delivery mechanism, and biological implications have been largely overlooked. This study demonstrates that BBB disruption by ICAHM generates a transient sterile neuroinflammatory response marked by increased production of cytokines, chemokines, and trophic factors leading activation of astrocytes, microglia, and macrophages. Additionally, unilateral ICAHM generates plasma increases in inflammatory molecules with evidence of sterile inflammation on the untreated contralateral hemisphere. These biological responses to ICAHM suggest its potential for immune modulation in several CNS pathologies.

Author contributions: S.R.B., C.N.K., L.L.M., E.A.N., and J.A.F. designed research; S.R.B., C.N.K., J.A.W., M.A.P., and M.S. performed research; S.R.B., C.N.K., J.A.W., and M.S. analyzed data; and S.R.B., C.N.K., L.L.M., E.A.N., and J.A.F. wrote the paper.

The authors declare no competing interest.

This article is a PNAS Direct Submission. D.M.H. is a guest editor invited by the Editorial Board.

[1]S.R.B. and C.N.K. contributed equally to this work.

[2]To whom correspondence may be addressed. Email: scott.burks@nih.gov or jfrank@cc.nih.gov.

This article contains supporting information online at https://www.pnas.org/lookup/suppl/doi:10.1073/pnas.2021915118/-/DCSupplemental.

Published April 27, 2021.

with cavitation detection may improve the capability for this sonication approach to induce BBBD in larger brain volumes (43).

Alternately, ICAHM is an effective method for hemispheric BBBD that has been safely used to enhance the delivery and efficacy of chemotherapy or targeted immunotherapeutics in treatment of CNS lymphoma and glioblastoma (16, 17, 20, 44–49). Furthermore, due to the localized infusion of chemotherapeutics or other agents following the mannitol infusion, ICAHM allows an increased concentration of therapeutics to CNS tumors while limiting systemic toxicity. It has been reported that ICAHM has been safely performed in over 700 brain tumor patients for a total of over 7,300 BBBD procedures (10). ICAHM BBBD with chemotherapy improves survival in chemosensitive brain tumors in the absence of cognitive impairment and treatment-related deaths (10, 44, 47). Although, ICAHM has been in clinical use since the 1980s to enhance delivery of chemotherapeutics, there have been few investigations into the changes in the molecular and immune cell responses in the brain parenchyma. Owing to the ready clinical implementation of ICAHM, this study sought to investigate and characterize potential SIR and immunomodulation following ICAHM BBBD.

This study investigated the temporal proteomic and transcriptomic changes in the rat brain following ICAHM-induced BBBD. Within 48 h, ICAHM BBBD induced an SIR in the treated hemisphere. Importantly, CCTF were detectable in serum and corresponded to a delayed SIR in the contralateral cortex. Overall, the results indicate that ICAHM BBBD induces an SIR and immune cell changes that can last 2 to 4 d.

Results

BBBD following ICAHM. Saline or HM was infused into the right internal carotid artery of Long Evans (LE) ($n = 58$) and Sprague–Dawley (SD) rats ($n = 24$). Animals were then euthanized at 0 (saline control), 0.083 (5 min), 0.5, 2, 6, 24, 48, and 96 h for proteomic and/or transcriptomic evaluations and at 6, 24, 48, and 96 h for histological examination (Fig. 1*A*). Macroscopic evaluation of Evans Blue administered immediately prior to BBBD revealed barrier opening throughout the right carotid artery distribution in all animals. Brains displayed variable staining intensity associated with the time interval post infusion (Fig. 1*B*). There was no indication of microhemorrhages post-ICAHM upon ex vivo MRI at 7 Tesla, which were devoid of hypointense voxels within the brains (34) (Movies S1–S3).

Proteomic Responses to ICAHM BBBD.

Proteomic response to ICAHM in the ipsilateral hemisphere. Brain homogenates from ICAHM-treated, contralateral, and saline control hemispheres were analyzed by multi- and single-plex enzyme-linked immunosorbent assays (ELISA) to determine differences in protein concentrations between treatment groups. Following ICAHM BBBD, significant changes in protein expression compared to saline controls ($P < 0.05$, ANOVA) were identified that were consistent with the development and subsequent resolution of an SIR. Notable changes included up-regulation of DAMPs, pro- and anti-inflammatory CCTFs, and chemotactic agents, with a concurrent increase in neuroprotective factors and down-regulation of proteins critical for BBB integrity. The proteomic changes began within 0.083 h post–ICAHM infusion with significant increases ($P < 0.05$ ANOVA) in interleukin (IL) 1β, IL2, IL12(p70), leptin, fractalkine, regulated on activation, normal T cell expressed and secreted (RANTES), and tumor necrosis factor alpha (TNFα) in ipsilateral BBBD tissue relative to sham-treated controls (Fig. 2 and *SI Appendix*, Fig. S1). From 0.5 to 6 h with significant increases in DAMPs and proinflammatory factors (IL1α, IL6, interferon gamma-induced protein 10 [IP-10], INFγ, stromal cell-derived factor-1 [SDF-1], heat shock protein [HSP] 70, and erythropoietin [EPO]) and chemotactic factors (granulocyte colony stimulating factor [G-CSF], granulocyte macrophage colony stimulating factor [GM-CSF], eotaxin, monocyte chemoattractant protein-1 [MCP-1], and macrophage inflammatory protein-1α). Several of the elevated stress reactive proinflammatory proteins (IL1α, IL6, IL18, IP-10, MIP1α, RANTES, TNFα, and EPO) remained significantly increased over 48 h, before declining to baseline levels by 96 h. At the 48 h time point, significant increases in several anti-inflammatory CCTF proteins (i.e., IL4, IL5, IL10, and IL13) were identified, supporting active resolution of the SIR. In addition to changes in inflammatory proteins, proteins impacting TJP integrity were significantly down-regulated, reflecting prolonged alterations in vascular dynamics following the initial acute ICAHM BBBD (Fig. 2 and *SI Appendix*, Fig. S1). Over the first 24 h, there was increased expression of proteins known to impact endothelial function including TNFα, IFNγ, EPO, MCP1, vascular endothelial growth factor (VEGF), and cell adhesion molecule (VCAM) as well as down-regulation of proteins directly impacting BBB integrity including occludins, claudin-5, and zonulae occludins 1(ZO1/TJP1). TJP levels returned toward control levels over 48 h. No significant changes in IL17, keratinocytes-derived chemokine (KC), lipopolysaccharide-induced CXC chemokine, MIP2, or brain-derived neurotrophic factor (BDNF) were observed over 96 h after BBBD.

To assess whether the parenchymal proteomic changes observed following ICAHM were strain dependent, expression of a subset of these proteins was measured at 2, 24, and 48 h post-ICAHM in the ipsilateral hemispheres of SD and LE rats (*SI Appendix*, Fig. S4). In both SD and LE, ICAHM BBBD resulted in Evans Blue extravasation into the ipsilateral hemisphere along with an SIR with similar changes in proinflammatory CCTF lasting from 2 to 48 h. These findings are consistent with the SIR occurring independent of rodent strain and applicable across a heterogeneous population.

Proteomic changes to ICAHM in serum and the contralateral hemisphere. Changes in CCTF and CAM in the serum of mannitol-treated or saline-control rats (Fig. 2*C* and *SI Appendix*, Fig. S3) were also evaluated at 0 (sham), 0.083, 0.5, 6, and 24 h post-ICAHM by multi- and single-plex ELISA. Within 30 min following BBBD, significant elevations in IL6, IL10, IFNγ, G-CSF, GM-CSF, KC, Eotaxin, EGF, MIP1α, MIP2, and VEGF were observed in the sera from disrupted rats compared to sham controls. Sham blood did not contain detectable quantities of IL6, GM-CSF, KC, or EGF, and therefore, the fold changes were calculated by generating minimal control values for these proteins. From 6 to 24 h, pro- and anti-inflammatory CCTFs were elevated, coinciding with increased expression in the ipsilateral parenchyma following BBBD (Fig. 2). Certain CCTFs were not detected from 6 to 24 h in the serum including IL6, GM-CSF, KC, and EGF. Interestingly, glial fibrillary acid protein (GFAP), presumably shed from intact or activated astrocytes, was only detected at significant levels within 30 min post-ICAHM and subsequently returned to baseline. The early changes in CCTF, CAM, and TJP in the ipsilateral brain following BBBD could account for leakage of CCTF into the circulation.

The presence of elevated CCTF in the blood following ICAHM BBBD led to the investigation of molecular changes in the contralateral hemisphere that did not show evidence of Evan's Blue extravasation (Figs. 1*B* and 2*B* and *SI Appendix*, Fig. S2). Analysis of CCTF, CAM, and TJP in the contralateral hemisphere from 2 to 96 h demonstrated similar patterns of significantly increased inflammatory protein expression similar to what was observed in the ipsilateral hemisphere (Fig. 2 *A* and *B* and *SI Appendix*, Figs. S1 and S2). The most significant fold increases were observed in the proinflammatory proteins IL1α, IP-10, MCP-1, MIP1α, and RANTES at 24 to 48 h post-HM infusion. At 96 h, all significantly elevated proteins were down trending, but IL1α, IP-10, MCP1, MIP1α, RANTES, and EGF remained significantly elevated compared to the ipsilateral hemisphere, where only IP-10 remained elevated. Similar to the ipsilateral hemisphere, TJPs (claudin-5, occludin, and ZO1/TJP1) significantly decreased; however, these results occurred at 24 and 48 h post-BBBD, whereas these changes

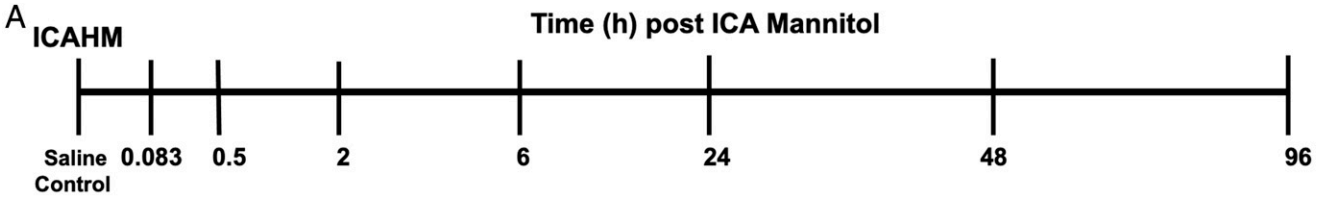

Time (h)	Saline	0.083	0.5	2	6	24	48	96
Proteomics Brain Ip/Con	+	Ip	Ip	Ip/Con	Ip/Con	Ip/Con	Ip/Con	Ip/Con
Proteomics Serum	+	+	+		+	+		
RNAseq	+	+	+	+	+	+		
Histology					+	+	+	+

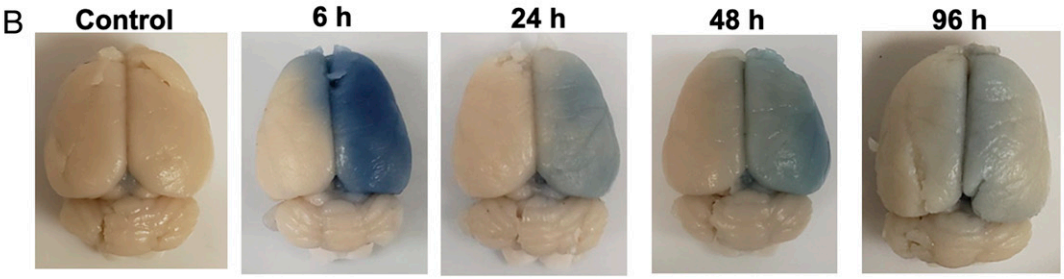

Fig. 1. Experimental design and analyses following rat BBBD by ICAHM. (*A*) Timeline of when samples of brain or serum were acquired for proteomic, RNA sequencing, or histological analysis following ICAHM BBBD. (*B*) Representative examples of rat brains with extravasated Evans blue following ICAHM at different time points that were used for histological and MRI analyses.

were observed in the ipsilateral hemisphere as early as 0.083 h (Fig. 2). Comparing the fold changes in CCTF, CAM, and TJP between the ipsilateral to contralateral hemispheres revealed significant differences in the magnitudes and timing of changes for CCTF, CAM, and TJP detected between 2 and 24 h timepoints (*SI Appendix*, Fig. S5). The proteomic results are consistent with local SIR within the parenchyma of both hemispheres with a delayed onset in the contralateral hemisphere compared to the ipsilateral hemisphere (Fig. 2 and *SI Appendix*, Figs. S1, S2, and S5).

Gene Expression Alterations after ICAHM BBBD. Paired-end next-generation sequencing of isolated RNA from brain homogenates identified 13,034 transcripts in ICAHM BBBD rats and sham control rats. Collectively, the alterations in expression of genes associated with endothelial cell function, tight junctional formation, and neuroinflammation revealed expression trends that were consistent with proteomic observations. Evaluation of the transcripts that encode key proteins from the proteomic studies demonstrated a pattern of early (less than 2 h post BBBD) and late (2 h and greater post-BBBD) transcriptional changes (Fig. 3). Early genes included increased transcription of genes encoding junctional proteins (Ocln and Tjp1), regulating adhesion to endothelial cells (Vcam1), and several inflammatory chemokine ligands (Cxcl1 and Cxcl12). Late genes included enhanced expression of an additional endothelial adhesion molecule (Icam1) and proinflammatory factors (Il1a, Il1b, Il6, Ccl2, CCL3, Cxcl1, Cxcl2, Cxcl10, and Tnf).

To explore gene expression patterns within the entire transcriptome, principal component analysis (PCA) was performed, demonstrating the most significant variance at 24 h post-ICAHM compared to sham-treated controls and all other time points (*SI Appendix*, Fig. S6). Hierarchical clustering of the entire transcriptome supported that the greatest transcriptional changes occurred at the 24 h time point, exhibiting clustering of all 24 h samples in the dendrogram (*SI Appendix*, Fig. S6). Further transcriptional analysis therefore focused on evaluating the patterns of transcriptional variation 24 h post-ICAHM.

Applying gene set enrichment analysis (GSEA), transcription-level evidence of biological pathway alterations was explored at 24 h post-ICAHM compared to sham controls (Fig. 4). Probing the gene ontology (GO) biological processes, curated gene sets revealed patterns consistent with an enhanced immune response as well as DNA, RNA, and protein biogenesis, repair, and modification (Fig. 4*A*). Focusing on the more selectively curated Hallmark gene sets demonstrated significant enhancement in the MYC targets, IFNγ response, IFNα response, IL6-JAK-STAT3 signaling, and allograft rejection gene sets at 24 h compared to sham controls (Fig. 4*B*). Hierarchical clustering of these significantly enriched Hallmark gene sets across all time points reveals these changes develop most robustly 24 h post BBBD and not at earlier time points (Fig. 4*C*). Collectively, these patterns support the development of a sterile inflammatory process and functional BBB changes with local enhanced transcription of genes contributing to these responses 24 h post-IHCHM.

Histological Alterations following ICAHM BBBD. Immunofluorescent histological evaluations of the rat brain following ICAHM were performed at 6, 24, 48, and 96 h on three to six adjacent sections. Tissues were evaluated for changes in the various cell components including NeuN (neurons), GFAP (astrocytes), Iba1 (microglia), CD68 (monocytes/macrophages/microglia), Glut 1, VCAM, and activated (cleaved) Caspase-3 on endothelium and complement 5B-9 (C5B-9) as evidence of BBBD. Fig. 5 qualitatively demonstrates the leakage of active C5B-9 into the parenchyma and on

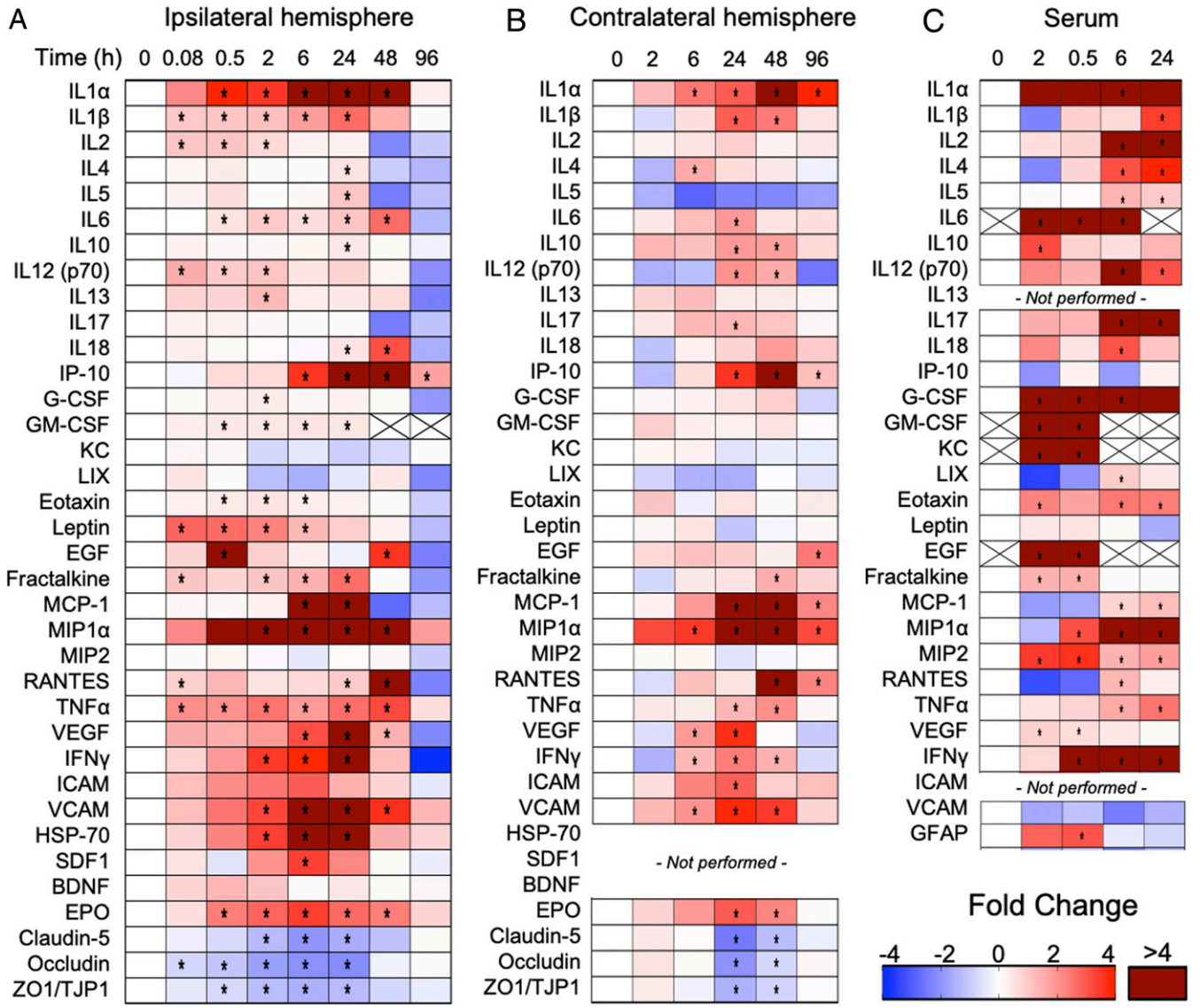

Fig. 2. Proteomic changes in the brain and serum following ICAHM infusion. Heat maps depict fold changes of CCTF, CAM, and TJP at select time points compared to sham saline control rats for ipsilateral ICAHM-exposed brain (*A*), contralateral brain (*B*), and serum (*C*) obtained at time of euthanasia ($n = 5$ rats per timepoint). Fold changes were determined from protein levels normalized to the sham control (time point = 0 h) for the ipsilateral hemisphere, contralateral hemisphere, and serum independently. Asterisks indicate statistically significant elevations ($P < 0.05$) identified by ANOVA and Bonferroni post hoc tests. Boxes containing Xs for specific CCTF were not detected by ELISA. *SI Appendix*, Figs. S1–S3 contain primary expression data.

the abluminal surface of the endothelium from 6 to 48 h time points in the ipsilateral cortex to ICAHM and at 24 to 48 h on the contralateral cortex. Histological confirmation of VCAM elevation based on ELISA of tissue homogenates was observed on the activated adluminal endothelial surfaces (Fig. 6). The increase in VCAM was apparent in the cortices over the 96 h and would be consistent expression of various proinflammatory CCTF in the blood and parenchyma. We observed increased activation of caspase 3 in endothelial cells from both the ipsilateral and contralateral hemispheres at 24 and 48 h post-ICAHM (Fig. 5), which may reflect the increase in stress from either circulating or parenchymal CCTF. Significant elevations in GFAP ($P = 0.02$ by ANOVA) and $CD68^+$ cells ($P = 0.017$ by ANOVA) were observed at 48 h following ICAHM based on immunofluorescence microscopy (Fig. 7). There was also a trend of elevation for Iba1 at 48 h ($P = 0.054$ by ANOVA), with significant Iba1 elevations at 96 h ($P = 0.009$ by ANOVA). To further identify $CD68^+$ cells in treated brains 48 h post-ICAHM, dual immunostaining for CD68 and Iba1 was performed, and $CD68^+$ cells were examined for Iba1 positivity. The mean distribution of $CD68^+$ cells was 79.1% $CD68^+$/$Iba1^+$ (microglia) and 20.9% $CD68^+$/$Iba1^-$ (monocytes/macrophages). $CD4^+$ and $CD8^+$ lymphocytes were undetected by immunofluorescence microscopy at any time points (*SI Appendix*, Fig. S7), suggesting that ICAHM did not induce an adaptive immune response.

Discussion

Transient opening of the BBB with ICAHM is a Food and Drug Administration–approved technique to deliver agents across the BBB with the ability to achieve hemispheric disruption in patients with CNS malignancies (clinicaltrials.gov: NCT01269853, NCT00253721, NCT02861898, NCT02819479, NCT00303849, and NCT00293475) (16–20) and has been associated with minimal adverse events (10, 50). ICAHM BBBD is thought to alter the metabolism and structure of the vascular endothelium due to osmotic shrinkage (18, 22, 23, 51–54), influencing changes in

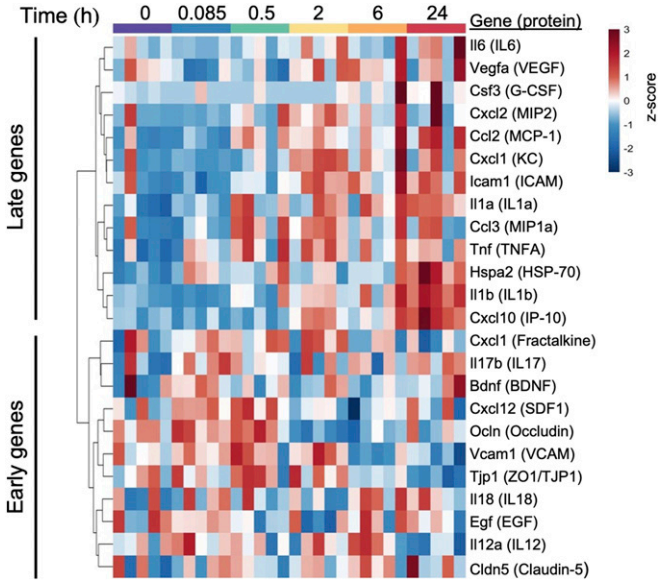

Fig. 3. Changes in transcripts encoding key proteins from the protein array following ICAHM infusion. Heat map is shown with hierarchical clustering of transcripts (*y*-axis) from each sample collected 0.085, 0.5, 2, 6, and 24 h post-ICAHM and sham control samples (*x*-axis) ($n = 5$ rats per timepoint). Gene expression values were log2 transformed and z-score normalized by gene. Dendrogram was constructed using Euclidean distance measure with hierarchical cluster analysis by Ward's method.

intracellular calcium that can translate into disruption of tight junctions, increased endothelial caveolae and transcytosis, and leakage of intravascular molecules into the parenchyma that can be visualized by contrast-enhanced MRI of the brain (55–57). In addition, ICAHM transiently alters the NVU with astrocytic swelling and separation of foot processes from the capillary endothelium (56, 58). However, molecular analysis and evaluation of immunologic changes following ICAHM have not been previously examined. In this study, we investigated molecular changes at the transcriptional and translational levels following ICAHM and demonstrated that a robust SIR begins within minutes of ICAHM, continues to develop over 48 h, and resolves by 96 h. Specifically, we found evidence for 1) proteomic changes in both ipsilateral and contralateral hemispheres and blood along with 2) genomic changes in the ipsilateral hemisphere supportive of 3) an SIR-enhanced expression of neuroprotective factors and 4) changes in the endothelium consistent with promoting transient vascular permeability.

Proteomic, transcriptomic, and immunofluorescence analyses of ipsilateral BBBD following ICAHM demonstrated the robust development of subsequent resolution of an SIR over the course of 96 h. Within 2 h post-ICAHM, increased expression of DAMPs (e.g., IL1α, HSP 70) along with IL1β, IL2, IL6, IL12p70, TNFα, IFNγ, and EPO were associated with BBBD and the SIR. Albumin (detected by Evans Blue staining) and complement C5B-9 in the ipsilateral hemisphere at 24 to 48 h would contribute to release of CCTF from the NVU into the microenvironment (59). While not measured in this study, fibrinogen is also a potent activator of CNS inflammation following BBBD (60). The acute increases in proinflammatory DAMPS and CCTF are likely due to protein influx from the circulation across the disrupted BBB as well as release of preformed factors in acute-responding immune cells (8, 59, 61, 62). Transcriptomic analysis demonstrated that elevations in genes for Tnf, Il1a, Il1b, Ccl2, Cxcl1, and Nfkb1 at 24 h indicate activation of NFκB-associated pathways, which are observed with injury and ischemia to the NVU (28, 29, 35, 36, 53, 63).

RNA sequencing pathway analyses at 24 h post-ICAHM demonstrated significant activation of both IFNα- and IFNγ-signaling pathways as well as those involved in IL6-JAK-STAT3 signaling, which can promote a local proinflammatory microenvironment, as evidenced by the delayed increases in GFAP and Iba1 observed by immunohistochemistry. Interestingly, there was minimal difference in astrocytic GFAP and microglial Iba1 in both hemispheres within 24 h post-ICAHM, possibly reflecting the presence of circulating and parenchymal CCTF. This time course of astrocytic and microglial activation was delayed in ICAHM BBBD compared to pFUS+MB, in which Iba1 was elevated at 1 to 6 h and GFAP at 6 to 24 h, as opposed to the current in which study elevations were observed only at 48 h (21). pFUS+MB BBBD was also associated with significant increases in CCTF and ICAM starting at 5 min in the SD rat cortex and returned to baseline levels by 24 h (21). In addition, ICAHM BBBD resulted in the significant expression in IL 4, IL10, and IL13, which could limit BBB opening and the extent of damage within the parenchyma (5, 54, 64–66). The delayed increase in neurotrophic factors EPO (67), SDF1α (68), VEGF (69), and GM-CSF (65) in the parenchyma could also provide neuroprotection and stimulate neurogenesis to areas of BBBD (70–72). Another point of interest is that pathway analyses indicated enrichment of IFNα pathways following ICAHM BBBD. There is scant investigation of these pathways in the absence of pathogens, but it is possible these pathways could have important immunomodulatory functions that would be relevant to clinical implementation of ICAHM BBBD. Further investigation linking transcriptomic results and protein expression within the parenchyma is warranted.

The alterations in inflammatory factors observed herein can promote the influx of systemic immune cells. Acute (i.e., 5 to 30 min) elevations in TNFα, IL1α, IL1β, and IL2 could induce chemoattractants (MCP1, GM-CSF, MIP1α, and RANTES) and generate an influx of systemic $CD68^+$ immune cells into the ipsilateral BBBD but not the contralateral hemisphere at 48 h (Fig. 7) (65, 73, 74). A distinct population of $CD68^+$/$Iba1^-$ cells was detected in the treated hemispheres at 48 h, suggesting they could be monocytes or macrophages (75), but it is unknown whether these activated cells were resident macrophages within the parenchyma prior to ICAHM or whether they infiltrated from the blood following the procedure. Of note, transient BBBD using pFUS+MB resulted in infiltration of systemic innate immune cells into the brain (21). It is also unclear why the contralateral hemisphere did not experience an increase in $CD68^+$ cells despite elevated CCTF, which might represent differences in the magnitudes of CCTF and/or CAM responses. Further investigations are required to determine the relationship between ICAHM BBBD and the homing of the innate immune cells into the parenchyma. Moreover, transcriptomic results from the contralateral hemisphere may provide insight into the different regional responses in the brain.

Increased CCTF in the blood may also contribute to the molecular changes in the contralateral hemisphere. Proteomic analysis of the contralateral hemisphere compared to saline controls revealed unexpected increases in CCTF and CAM. Possible explanations for this finding include the following: 1) ICAHM passed through the Circle of Willis and activated contralateral endothelial cells resulting in an SIR, 2) TNFα, IL1α, and IL1β propagated through the ipsilateral parenchyma into the cerebrospinal fluid (CSF) and altered homeostasis of the contralateral hemisphere (76), and/or 3) functional alteration of the ipsilateral endothelial barrier lead to leakage of CCTF into the systemic circulation via glymphatic drainage through the CSF into the arachnoid granulations and dural sinuses or via draining cervical lymph nodes (77–81). In CNS lymphoma patients receiving ICAHM with chemotherapy, blood samples before and after BBBD demonstrated significant elevations of S100β and α2 macroglobulin originating from the parenchyma at 4 h (82). S100β along with GFAP are biomarkers that can be found in blood following injury (83, 84). GFAP is part of the astroglia skeleton, and

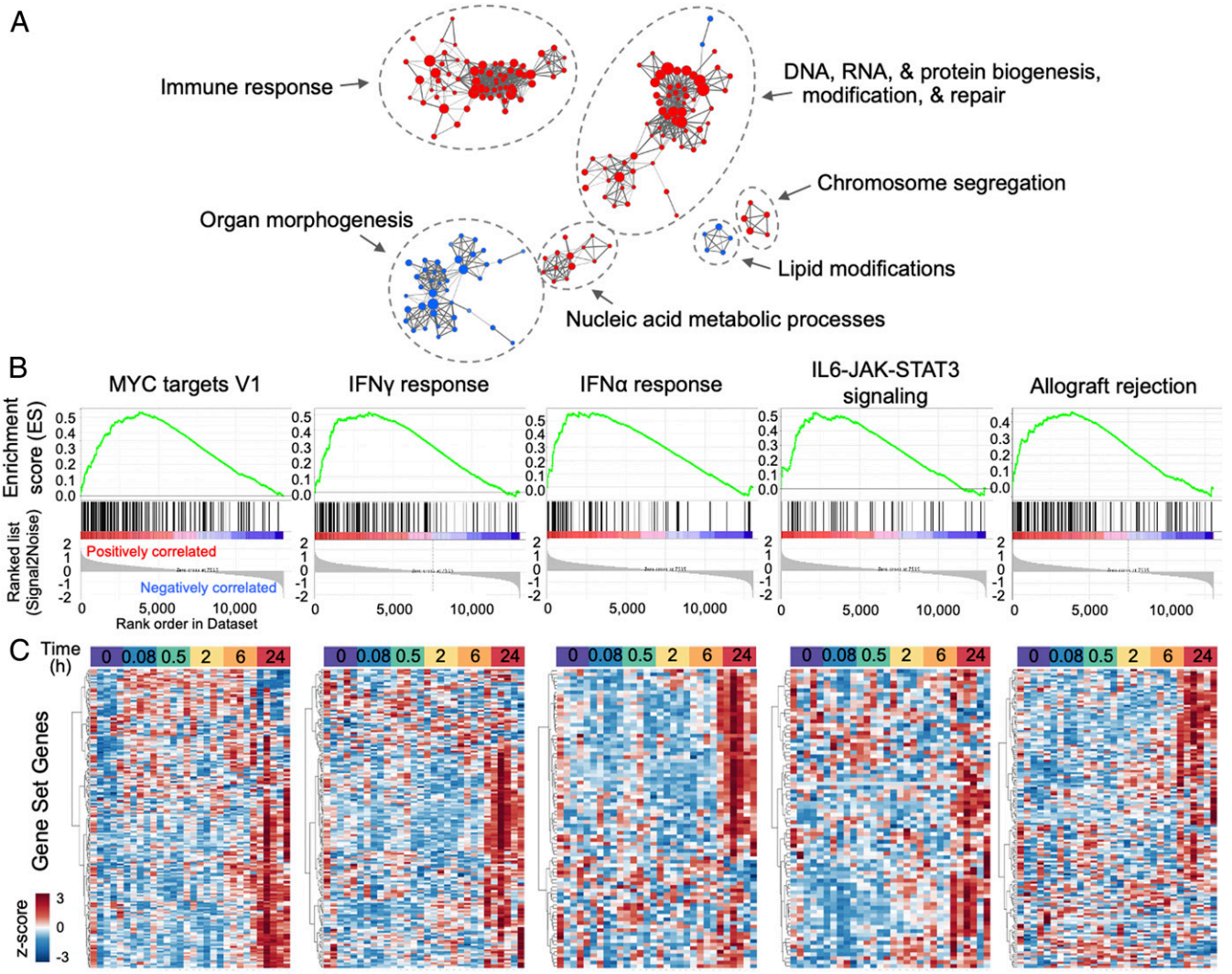

Fig. 4. Gene set enrichment patterns at 24 h post-ICAHM infusion in ipsilateral brain. (*A*) Enrichment map visualizations of GSEA demonstrating GO biological processes enriched at 24 h post–ICAHM BBBD relative to controls (n = 5 rats per timepoint). Nodes represent GO terms. Functionally related clusters were manually circled and labeled. Node color represents direction of enrichment (Red: up-regulation; Blue: down-regulation). Node size is proportional to the number of genes within each GO term. Edge thickness signifies degree of overlap between GO terms (number of genes shared between two gene sets). (*B*) Enrichment plots of the top five significantly (FDR q-value <0.05 with NES >2.0) enriched hallmark gene sets at 24 h post ICAHM BBBD compared to controls. NES: normalized enrichment score; FDR: false discovery rate. (*C*) Hierarchical clustering of genes (*x*-axis) that define the top significantly hallmark gene sets identified above. Gene expression patterns across samples from all time points (*y*-axis) demonstrate prominent up-regulation in samples collected 24 h post-BBBD. Transcriptional expression values were log2 transformed and z-score normalized by gene. Dendrogram was constructed using Euclidean distance measure with hierarchical cluster analysis by Ward's method.

the transient elevation observed in the blood following ICAHM may result from the increase in perivascular edema that stretches or removes astrocytic endplates from the endothelium (58). Further investigation will be needed to determine whether temporal transcriptomic differences exist between hemispheres following ICAHM BBBD. Tweezing out the contributions of the various cellular components of the NVU to the SIR in response to ICAHM will require monitoring of temporal changes by signal-cell RNA sequencing.

The mechanisms by which ICAHM BBBD induces the observed changes in rat brain have not been fully elucidated. ICAHM transiently alters the NVU with astrocytic swelling and separation of foot processes from the capillary endothelium and alteration in TJP expression (56, 58, 85). Capillary shrinkage has been associated with increasing doses of ICAHM and DNA damage (terminal deoxynucleotidyl transferase dUTP nick end labeling positivity) of the endothelium (65, 86), which was not observed in the current study. However, TJP claudin-5, ZO1, and Occludin were significantly decreased following ICAHM, acutely in the ipsilateral and delayed in the contralateral hemispheres. In vitro exposures of endothelial cells to HM at clinical concentrations result in intracellular Ca^{2+} increases and apoptosis associated with activation tyrosine and stress kinases, as well as focal adhesion contact-associated proteins (86). Intracellular Ca^{2+} serves as second messenger involved in regulation of BBB function and TJP integrity and the changes in concentration to vasoactive and proinflammatory CCTF (86, 87). It is possible that the dynamic alteration in blood osmolarity during ICAHM that results in cellular deformation induces mechanotransduction through intracellular Ca^{2+} signaling (64, 65). The increase in cytosolic Ca^{2+} initiates a cascade of events including increases in reactive oxygen species, nitric oxide, ATP levels, activation of Rho-A–activated kinase, mitogen-activated protein kinase, and NFκB pathways that leads to decreased expression and reorganization of TJP (86, 87). The elevation of TNFα, MCP 1, and VEGF in the parenchyma and circulation

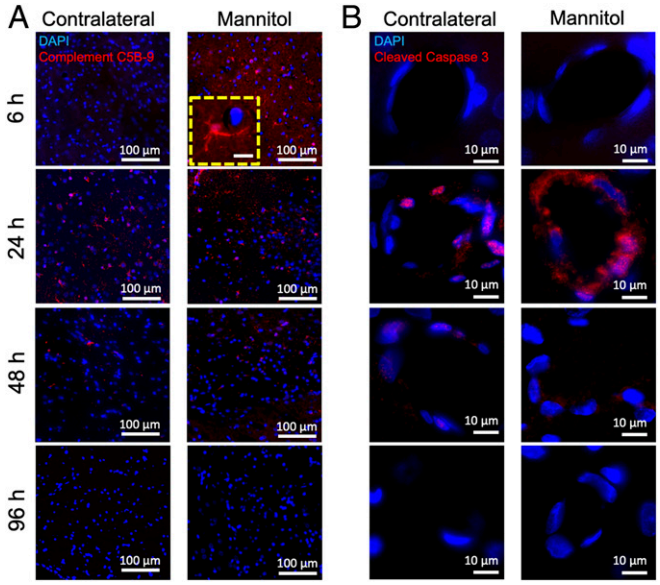

Fig. 5. Immunohistochemistry for complement C5B-9 and activated caspase-3. Immunofluorescence staining of the contralateral and ipsilateral (mannitol) hemispheres of rat brain (n = 3 rats per timepoint) at 6, 24, 48, and 96 h post–ICAHM BBBD. There is enhanced staining for (*A*) complement C5B-9 and (*B*) cleaved caspase-3 in capillaries, particularly at the 24 h time point. DAPI (blue) represents nuclear staining. (Scale bars, 100 μm for *A* [inset, 10 μm] and 10 μm for *B*.)

likely contributed to delayed return of the TJP to baseline (88, 89) and supports the observation of increased cleaved caspase-3 in the endothelium of both hemispheres (90). TNFα and IL1β also stimulate human cerebral endothelium in vitro and cause the release of numerous proinflammatory factors and chemoattractants for up to 72 h along with increased expression of ICAM, VCAM, and soluble CAM (91).

ICAHM BBBD can be performed in both carotid artery in the rat and the carotid or vertebral arteries in humans (10). In rats, the ICAHM procedure can only be performed once, because the artery must be ligated after mannitol infusion (92). However, multiple BBBD procedures can be performed in patients; typically, two arterial circulations are opened once a month. The ICAHM procedure is a relatively straightforward, albeit invasive procedure, requiring the placement of intracarotid artery catheter under fluoroscopic guidance in an interventional radiology suite. Enhanced chemotherapy delivery using ICAHM BBBD procedure has been performed with minimal adverse events (10, 50).

ICAHM enhancing of both drug delivery and inducing SIR may have implications in the treatment of CNS diseases as well as infiltrative cancers. It is plausible that ICAHM BBBD–inducing DAMP and a transient SIR with activated microglia and the innate immune response could be harnessed to increase clearance of neurotoxic amyloid plaques along with Tau proteins similar to what has been observed with pFUS+MB (93–101). In experimental models of Alzheimer's disease (AD), single or multiple pFUS+MB BBBD treatments decrease the burden of amyloid β(Aβ) plaques and/or hyperphosphorylated Tau, which are accompanied by function clinical outcomes (93–101). The SIR following pFUS+MB BBBD activates microglia, resulting in increased clearance of Aβ plaques (96, 102, 103). Following investigation in large animal models of AD, translation of repeated ICAHM BBBD should be evaluated in clinically approved AD trials alone or in combination with neurotherapeutics.

In the current study, the lack of damage or antigen presentation in either hemisphere in the presence of the SIR was an insufficient stimulus to induce an adaptive immune response with influx of $CD4^+$ and $CD8^+$ lymphocytes into the brain. Early studies with checkpoint immune therapies have shown that more immunogenic tumors respond better to these immune modulating treatments than anergic tumors (104) such as glioblastomas which can have an immunosuppressive tumor microenvironment (TME) (105, 106). The induced SIR by ICAHM BBBD may sensitize the TME, enhancing or serving an adjunctive role to anti-tumor immunotherapies. Further investigations to evaluate the effect of ICAHM BBBD to determine whether the SIR can sensitize the CNS TME to potentially stimulate both innate and adaptive immune cellular responses alone or when combined with immunotherapy approaches enhance therapeutic outcomes.

There are a few limitations of this study that need to be addressed. Although we showed that ICAHM BBBD caused an SIR in normal rodents without CNS pathology, long-term follow-up of inflammatory status in the absence of confounding pathology could address potential for chronic CNS immune activation. Additionally, it would be important to determine whether ICAHM induces similar molecular and immune responses in brain tumor models and other CNS pathologies (i.e., AD), which would have compromised endothelial function, as well as in large animal models in which the technique could be performed multiple times. It is plausible that ICAHM BBBD SIR in CNS tumor models would accelerate an adaptive immune response shifting from an immunosuppressive to anti-tumor microenvironment, elevating the immune score based on the location of infiltrating cytotoxic T cells within the pathology (107, 108). It will be important to evaluate whether repeated ICAHM BBBD–induced SIR causes any pathological changes to the NVU in nonmalignant CNS pathologies (i.e., AD) that would allow rapid translation into clinical trials. ICAHM BBBD in combination with neurotherapeutic infusions has successfully and safely

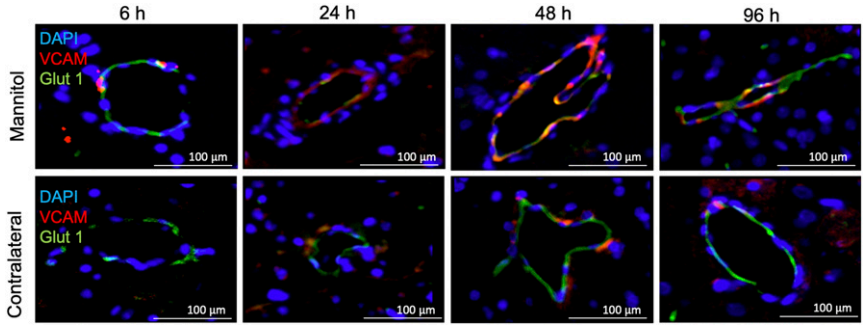

Fig. 6. Time course of VCAM expression in brain capillaries following ICAHM BBBD. Immunofluorescence staining of capillary endothelium in ipsilateral (mannitol) and contralateral hemispheres of rat brains (n = 3 rats per timepoint) at 6, 24, 48, and 96 h post–ICAHM BBBD. VCAM stain (red) colocalized with endothelial cells identified by Glut1 staining (green) from 6 to 96 h post ICAHM. (DAPI [blue] is nuclear stain; Scale bars, 100 μm.)

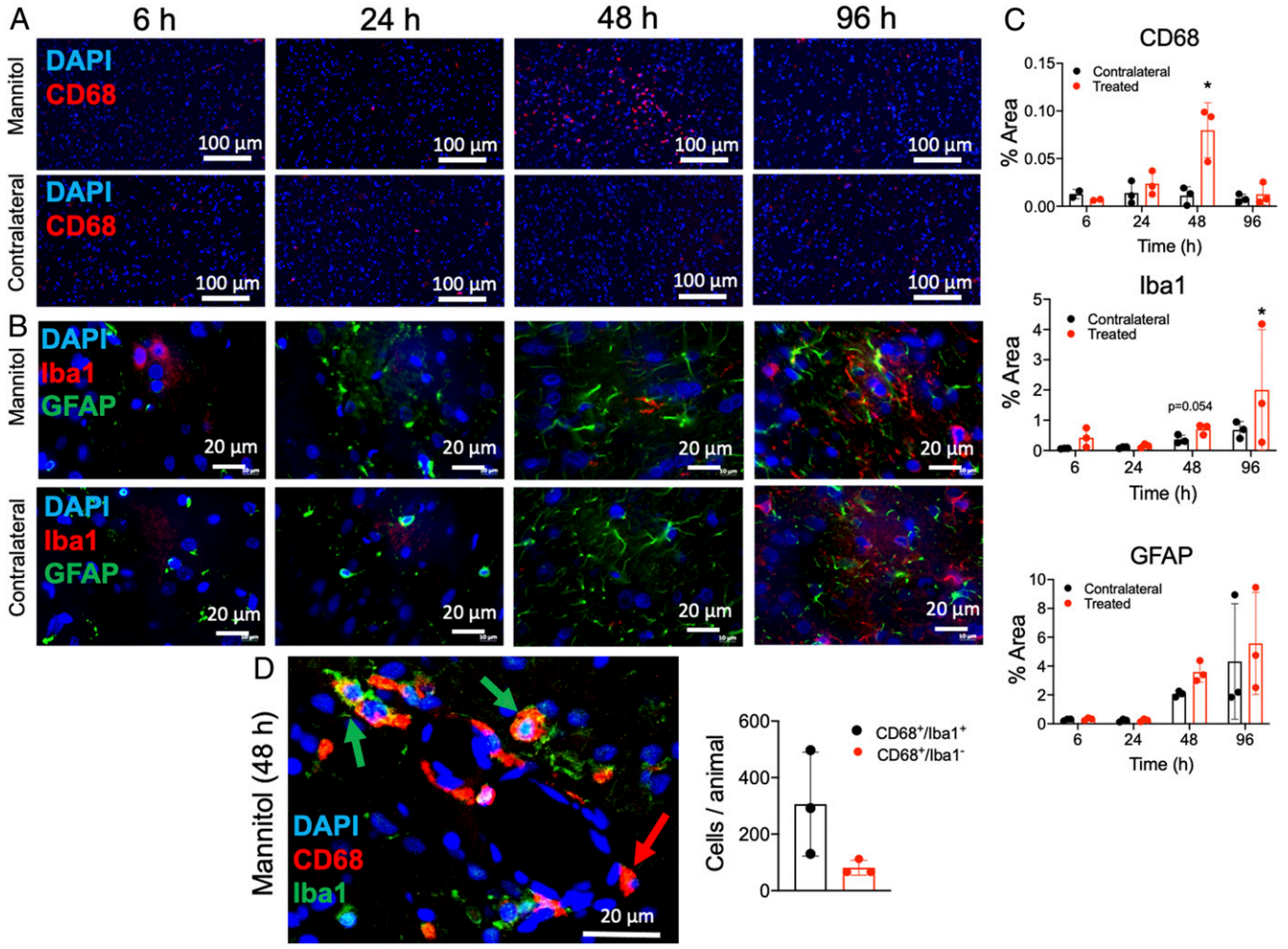

Fig. 7. Histological evaluation of the effect in the brain post-ICAHM. Immunohistochemical staining of the ipsilateral and contralateral brain at 6, 24, 48, and 96 h post–ICAHM BBBD revealed significant ($P < 0.05$) increase in (*A*) CD68 reactivity (red; monocytes/macrophages/microglia) and (*B*) GFAP reactivity (green; astrocytes) with a nonsignificant trend ($P = 0.054$) toward enhancement of Iba1 expression (red; microglia) in ICAHM-treated hemisphere compared to contralateral control at 48 h. (*C*) Quantitative analysis for $CD68^+$, GFAP, and Iba1 from HM-treated ipsilateral compared to contralateral hemisphere at 6, 24, 48, and 96 h. Normalized areas of positive fluorescence staining were calculated using ImageJ from 20 to 30 FOV in each hemisphere over three to five sections from each animal ($n = 3$ rats per timepoint except for the 6 h timepoint of the CD68 panel where $n = 2$ rats). (*D*) Representative image of CD68 (red) Iba1 (green) double staining from a treated hemisphere at 48 h post-ICAHM and quantification of $CD68^+/Iba1^+$ (microglia; green arrow) and $CD68^+/Iba1^-$ (monocytes/macrophages; red arrow) cells ($n = 3$ rats). Imaging in *D* was analyzed using automated cell selection and counting algorithms in Image J from 20 to 30 FOV per animal. Statistical analyses were based on ANOVA comparisons between normalized area of fluorescence between the two hemispheres. Scale bars, 100 µm in *A* and 20 µm in *B* and *D*. Images in *A* and *B* were acquired using a slide scanner that stitches multiple images from a slide into a single composite image. For presentation, features of interest may span multiple stitched images. Data in *C* and *D* are presented as mean ± STD.

been administered to patients with CNS malignancies (16, 17, 50). Further research is needed to determine how the molecular and pathological response to multiple ICAHM will impact the reparative or neurodegenerative processes in the brain and whether BBBD by ICAHM would increase or decrease susceptibility to subsequent cerebrovascular injury. We have found no evidence of long-term negative effects of ICAHM in patients, but potential positive effects have not been evaluated (10, 44, 45, 48). We were unable to identify which cellular components of the NVU that contribute to the SIR and future studies should address the events that initiate the changes in the microenvironment and whether there is an issue with high levels of CCTF in the circulation. Moreover, the temporal RNA sequencing data obtained following ICAHM BBBD in the current study has not undergone an in-depth exploration and therefore will require further evaluation. Lastly, with the significant decrease in TJP and increases in CCTF and CAM in the parenchyma at ~24 to 48 h post-ICAHM, it would be important to potentially visualize by quantitative T1 maps (109, 110) from contrast-enhanced MRI comparing results from multiple time points to determine the effect of the SIR on the integrity of the BBB.

In summary, ICAHM BBBD is a commonly employed approach for delivery of neurotherapeutics in the treatment of CNS malignancies. The SIR associated with this approach within the brain and serum along with the innate immune response should be exploited in combination with immune therapeutic approaches to stimulate an adoptive immune response in the treatment of CNS malignancies (111). Further research is needed into the possible clinical applications of ICAHM BBBD in stimulating immune responses in the treatment of CNS diseases.

Methods

Animal experiments were approved by the Institutional Animal Care and Use Committee and were supervised by the Department of Comparative Medicine, Oregon Health & Science University, Portland, OR (animal protocol IP0000843). Rats used for these studies were adult females weighing 200 to

270g, obtained from Charles River (https://www.criver.com/). LE rats (n = 58) were used for all experimental approaches. SD rats (n = 24) were used to confirm proteomic and transcriptomic findings. All rats were aged 3 to 6 mo at the time of procedures. Animals were entered into the study based on weight: the mean ± SD of the weights of LE rats was 239.7 ± 16.6 g and 235.4 ± 17.3 g for SD rats.

ICAHM and Evans Blue Perfusion. ICAHM infusion parameters were utilized that have been previously demonstrated to open blood tumor barrier and BBB in rats (112). Rats were anesthetized with isoflurane (5% induction, 2% maintenance Aerrane; Anaquest, Inc.) and then switched to 1.5 L/min of 50% N_2O and intravenous Propofol anesthesia (800 mg/kg/min; Zeneca Pharmaceuticals). A ventral neck incision was made, and the right external carotid artery was isolated at the level of the carotid bifurcation. A PE-50 polyethylene catheter filled with heparinized saline was tied into the right external carotid artery retrograde toward the bifurcation with the common carotid (92). Mannitol (22%) warmed to 37 °C was infused via the right external carotid artery catheter at a rate of 0.08 mL/s for 25 s, using a Harvard Instruments model 11-Plus constant flow pump (Harvard Apparatus, Inc.). The external carotid artery was ligated after mannitol infusion, and the skin was sutured closed. To provide a qualitative measure of the degree of disruption, Evans blue dye (2%, 2 mL/kg) was administered intravenously (IV) to all animals 5 min before BBBD to serve as a visual marker for BBBD and was assessed after euthanasia.

Proteomic Analyses. Frozen brain tissue (n = 5 per time point) was homogenized in a Tween-20–based lysis buffer containing protease inhibitors (Roche Diagnostics), and protein quantification was performed using bicinchoninic acid protein quantification assays (Thermo Fisher). Samples were diluted to a total of 2,000 μg/mL of total protein and analyzed by ELISA. Serum samples were analyzed directly without further modification. Multiplex ELISA for rat cytokines (Milliplex, Millipore Sigma) and single-plex ELISA for TJP1, Occludin, Claudin-5 (LS Bio), ICAM, VCAM (http://mybiosource.com), HSP70, SDF1, BDNF, and EPO (Raybiotech, Peachtree Corners) were performed according to manufacturer protocols. For heatmap presentation, ratios of concentration values at each time point to the mean values of sham control were calculated and expressed as fold changes. Proteins that were downregulated compared to controls (i.e., fold-changes between 0 and 1) were converted to negative numbers by dividing −1 by the ratio of treated:control.

RNA Sequencing and Analysis. Frozen brain tissue (n = 5 per time point) was homogenized and purified using column-based kits (PureLink RNA Mini Kits, ThermoFisher). A total of 1 μg of RNA was acquired from each sample. RNA quantity and quality were measured using gel electrophoresis (Experion RNA Analysis Kits, BioRad), and all samples were within one RNA quality indicator value of each other. Purified RNA was submitted to the NIH Intramural Sequencing Center, and paired-end messenger RNA sequencing was performed using a NovaSeq. 6000 (Illumina). Sequencing files were processed in Partek-Flow (Partek). Sequences were aligned using the STAR alignment tool (v2.5.3a), and both genes and transcripts were quantified using the Partek E/M quantification tool. Transcripts were normalized and filtered to remove transcripts with <30 counts.

PCA was performed on the 1,000 most-variable genes in the dataset on $\log_2$-transformed and z-score–normalized data matrix (FactoMineR and Factoextra R package) (113). Distance matrices were computed for $\log_2$-transformed and z-score–normalized expression data using the Euclidean distance measure and hierarchical cluster analysis by Ward's method (Factoextra R package) (113).

GSEA was performed on normalized counts to compare gene expression patterns at 24 h after osmotic BBBD relative to control gene expression data from non-BBBD brain tissue (114). GSEA was run applying default specifications, including the Signal2Noise ranking metric. Gene sets smaller than 15 genes and greater than 500 genes were excluded, and enrichment P values were estimated by 1,000 permutations and corrected for multiple testing using the Benjamini–Hochberg method. Analyzed gene sets were from the curated molecular signature database (MsigDB): Gene Ontology (C5; n = 4436) or Hallmark (H; n = 50) gene set collections, available at http://www.broadinstitute.org/gsea/msigdb/collections.jsp (115, 116).

GSEA results were visualized using the Enrichment Map plugin for Cytoscape (V2.8, http://www.cytoscape.org/) (117). For visualization purposes, nodes with conservative significance thresholds of P value <0.005 with a false discovery rate (FDR) q-value <0.1 were included. Clusters of functionally related enriched GO terms with ≥5 nodes were manually circled and labeled. In the largest cluster of significantly enriched nodes, representing immune processes, individual nodes with the most significant enrichment (FDR q-value <0.05 with a Normalized Enrichment Score [NES] >2) were individually depicted in list form by their GO gene set title.

Ex Vivo MRI. Ex vivo MRI was performed on a vertical bore 7 Tesla Bruker BioSpin Magnetic using a volume coil (Bruker, internal diameter 2 cm). Brains were immersed in susceptibility matching fluid (Fomblin, A-Tek LLC) and imaged with a T2* weighted three-dimensional Multiple Gradient Echo sequence (TR = 100 ms, TE = 5 ms [first echo], Echo Spacing = 5 ms, number of echoes = 10, Flip Angle = 30°, and Field of View [FOV] = 30 × 30 × 30 mm; Image Resolution = 100 × 100 × 100 μm with number of averages = 6).

Histological Staining. Rats (n = 3 per timepoint) were euthanized at 6, 24, 48, and 96 h post-ICAHM and were perfused with 4% paraformaldehyde and postfixed for 48 h. Fixed brains were embedded in paraffin and sectioned at 5 to 10 μm. Paraffin tissue sections were stained for immunohistochemistry. Sections were baked at 65 °C for 1 h and dewaxed in xylenes and rehydrated in graded ethanol solutions. Antigen retrieval was performed by boiling tissue in basic heat-induced epitope recovery citrate buffer (R&D Systems) and blocked with SuperBlock (Thermo Fisher). Slides were incubated with primary antibodies (see *SI Appendix*, Table S1 for catalog numbers and concentration) for 2 h at room temperature. Fluorescently labeled secondary antibodies were incubated for 1 h at room temperature. Slides were mounted using ProLong Diamond containing DAPI (ThermoFisher) and visualized using an epifluorescent slide scanner (AperioFL, Leica Biosystems) or epifluorescent microscope (Axio, Zeiss).

Histological Analyses. Between 20 and 30 FOVs from three animals in each group were acquired for each hemisphere. Images were analyzed using ImageJ (NIH) after thresholding each FOV image. The total area of the positive fluorescent signal was quantified in each FOV and normalized to the total area of the individual FOV. Normalized positive fluorescent signal was plotted for treated and contralateral as a percentage of total area. For Iba1/CD68 double-staining, thresholding for each stain was performed, and then cell-counting algorithms in ImageJ were used to quantify $CD68^+$ cells and determine numbers of $CD68^+/Iba^+$ and $CD68^+/Iba1^-$ cells.

Statistical Analyses. All values are presented as mean ± SD. Most statistical analyses were performed with Prism (version 8, GraphPad Software, Inc.). One-way ANOVA with Bonferroni post hoc tests were used for multiple comparisons. P values < 0.05 were considered significant. Statistical comparisons for transcriptomic data were performed using the gene-specific analysis (Partek Genomics Suite, Partek Inc.) comparing each time point to sham-treated brain tissue (represented as 0 h time point). For histological analysis, comparisons between hemispheres at each time point were performed with paired t tests with significant level $P < 0.05$.

Data Availability. All study data are included in the article and/or supporting information.

ACKNOWLEDGMENTS. This research was funded by the Intramural Research Programs of the Clinical Center and the National Institute of Biomedical Imaging and Bioengineering at the NIH (J.A.F.). This work was supported in part by NIH Grants CA199111 and CA137488, a Veterans Administration Merit Review Grant (BX003897), the Jonathan D. Lewis Foundation, and by the Walter S. and Lucienne Driskill Foundation (E.A.N.).

1. R. Daneman, A. Prat, The blood-brain barrier. *Cold Spring Harb. Perspect. Biol.* **7**, a020412 (2015).
2. Z. Zhao, A. R. Nelson, C. Betsholtz, B. V. Zlokovic, Establishment and dysfunction of the blood-brain barrier. *Cell* **163**, 1064–1078 (2015).
3. W. A. Banks, From blood-brain barrier to blood-brain interface: New opportunities for CNS drug delivery. *Nat. Rev. Drug Discov.* **15**, 275–292 (2016).
4. K. Schoknecht, Y. David, U. Heinemann, The blood-brain barrier-gatekeeper to neuronal homeostasis: Clinical implications in the setting of stroke. *Semin. Cell Dev. Biol.* **38**, 35–42 (2015).
5. F. L. Cardoso, D. Brites, M. A. Brito, Looking at the blood-brain barrier: Molecular anatomy and possible investigation approaches. *Brain Res. Brain Res. Rev.* **64**, 328–363 (2010).
6. H. L. McConnell, C. N. Kersch, R. L. Woltjer, E. A. Neuwelt, The translational significance of the neurovascular unit. *J. Biol. Chem.* **292**, 762–770 (2017).
7. A. Villabona-Rueda, C. Erice, C. A. Pardo, M. F. Stins, The evolving concept of the blood brain barrier (BBB): From a single static barrier to a heterogeneous and dynamic relay center. *Front. Cell. Neurosci.* **13**, 405 (2019).
8. Y. Serlin, I. Shelef, B. Knyazer, A. Friedman, Anatomy and physiology of the blood-brain barrier. *Semin. Cell Dev. Biol.* **38**, 2–6 (2015).

9. J. N. Sarkaria *et al*., Is the blood-brain barrier really disrupted in all glioblastomas? A critical assessment of existing clinical data. *Neuro-oncol.* **20**, 184–191 (2018).
10. N. D. Doolittle, L. L. Muldoon, A. Y. Culp, E. A. Neuwelt, Delivery of chemotherapeutics across the blood-brain barrier: Challenges and advances. *Adv. Pharmacol.* **71**, 203–243 (2014).
11. A. Abrahao *et al*., First-in-human trial of blood-brain barrier opening in amyotrophic lateral sclerosis using MR-guided focused ultrasound. *Nat. Commun.* **10**, 4373 (2019).
12. N. Lipsman *et al*., Blood-brain barrier opening in Alzheimer's disease using MR-guided focused ultrasound. *Nat. Commun.* **9**, 2336 (2018).
13. A. Carpentier *et al*., Clinical trial of blood-brain barrier disruption by pulsed ultrasound. *Sci. Transl. Med.* **8**, 343re2 (2016).
14. T. Mainprize *et al*., Blood-brain barrier opening in primary brain tumors with non-invasive MR-guided focused ultrasound: A clinical safety and feasibility study. *Sci. Rep.* **9**, 321 (2019).
15. S. H. Park *et al*., Safety and feasibility of multiple blood-brain barrier disruptions for the treatment of glioblastoma in patients undergoing standard adjuvant chemotherapy. *J. Neurosurg.*, 10.3171/2019.10.Jns192206 (2020).
16. R. S. D'Amico *et al*., Super selective intra-arterial cerebral infusion of modern chemotherapeutics after blood-brain barrier disruption: Where are we now, and where we are going. *J. Neurooncol.* **147**, 261–278 (2020).
17. S. Chakraborty *et al*., Superselective intraarterial cerebral infusion of cetuximab after osmotic blood/brain barrier disruption for recurrent malignant glioma: phase I study. *J. Neurooncol.* **128**, 405–415 (2016).
18. R. A. Kroll, E. A. Neuwelt, Outwitting the blood-brain barrier for therapeutic purposes: Osmotic opening and other means. *Neurosurgery* **42**, 1083–1099 (1998).
19. E. A. Neuwelt *et al*., Osmotic blood-brain barrier modification: Clinical documentation by enhanced CT scanning and/or radionuclide brain scanning. *AJR Am. J. Roentgenol.* **141**, 829–835 (1983).
20. S. A. Dahlborg *et al*., Non-AIDS primary CNS lymphoma: First example of a durable response in a primary brain tumor using enhanced chemotherapy delivery without cognitive loss and without radiotherapy. *Cancer J. Sci. Am.* **2**, 166–174 (1996).
21. Z. I. Kovacs *et al*., Disrupting the blood-brain barrier by focused ultrasound induces sterile inflammation. *Proc. Natl. Acad. Sci. U.S.A.* **114**, E75–E84 (2017).
22. R. R. Lonser, M. Sarntinoranont, P. F. Morrison, E. H. Oldfield, Convection-enhanced delivery to the central nervous system. *J. Neurosurg.* **122**, 697–706 (2015).
23. E. Neuwelt *et al*., Strategies to advance translational research into brain barriers. *Lancet Neurol.* **7**, 84–96 (2008).
24. A. R. Rezai *et al*., Noninvasive hippocampal blood-brain barrier opening in Alzheimer's disease with focused ultrasound. *Proc. Natl. Acad. Sci. U.S.A.* **117**, 9180–9182 (2020).
25. K. Hynynen, N. McDannold, N. Vykhodtseva, F. A. Jolesz, Noninvasive MR imaging-guided focal opening of the blood-brain barrier in rabbits. *Radiology* **220**, 640–646 (2001).
26. N. McDannold, N. Vykhodtseva, K. Hynynen, Effects of acoustic parameters and ultrasound contrast agent dose on focused-ultrasound induced blood-brain barrier disruption. *Ultrasound Med. Biol.* **34**, 930–937 (2008).
27. L. P. Cacheaux *et al*., Transcriptome profiling reveals TGF-beta signaling involvement in epileptogenesis. *J. Neurosci.* **29**, 8927–8935 (2009).
28. S. P. Gadani, J. T. Walsh, J. R. Lukens, J. Kipnis, Dealing with danger in the CNS: The response of the immune system to injury. *Neuron* **87**, 47–62 (2015).
29. R. Shechter, M. Schwartz, CNS sterile injury: Just another wound healing? *Trends Mol. Med.* **19**, 135–143 (2013).
30. S. Álvarez, M. A. Muñoz-Fernández, TNF-A may mediate inflammasome activation in the absence of bacterial infection in more than one way. *PLoS One* **8**, e71477 (2013).
31. D. Amantea *et al*., Rational modulation of the innate immune system for neuroprotection in ischemic stroke. *Front. Neurosci.* **9**, 147 (2015).
32. G. Y. Chen, G. Nuñez, Sterile inflammation: Sensing and reacting to damage. *Nat. Rev. Immunol.* **10**, 826–837 (2010).
33. P. Ludewig, J. Winneberger, T. Magnus, The cerebral endothelial cell as a key regulator of inflammatory processes in sterile inflammation. *J. Neuroimmunol.* **326**, 38–44 (2019).
34. Z. I. Kovacs *et al*., MRI and histological evaluation of pulsed focused ultrasound and microbubbles treatment effects in the brain. *Theranostics* **8**, 4837–4855 (2018).
35. G. Singhal, E. J. Jaehne, F. Corrigan, C. Toben, B. T. Baune, Inflammasomes in neuroinflammation and changes in brain function: A focused review. *Front. Neurosci.* **8**, 315 (2014).
36. R. M. Ransohoff, V. H. Perry, Microglial physiology: Unique stimuli, specialized responses. *Annu. Rev. Immunol.* **27**, 119–145 (2009).
37. K. Hynynen, N. McDannold, N. Vykhodtseva, F. A. Jolesz, Non-invasive opening of BBB by focused ultrasound. *Acta Neurochir. Suppl. (Wien)* **86**, 555–558 (2003).
38. D. E. Goertz, An overview of the influence of therapeutic ultrasound exposures on the vasculature: High intensity ultrasound and microbubble-mediated bioeffects. *Int. J. Hyperthermia* **31**, 134–144 (2015).
39. D. McMahon, R. Bendayan, K. Hynynen, Acute effects of focused ultrasound-induced increases in blood-brain barrier permeability on rat microvascular transcriptome. *Sci. Rep.* **7**, 45657 (2017).
40. D. McMahon, K. Hynynen, Acute inflammatory response following increased blood-brain barrier permeability induced by focused ultrasound is dependent on microbubble dose. *Theranostics* **7**, 3989–4000 (2017).
41. Z. I. Kovacs, S. R. Burks, J. A. Frank, Focused ultrasound with microbubbles induces sterile inflammatory response proportional to the blood brain barrier opening: Attention to experimental conditions. *Theranostics* **8**, 2245–2248 (2018).
42. M. Schwartz, A. Deczkowska, Neurological disease as a failure of brain-immune crosstalk: The multiple faces of neuroinflammation. *Trends Immunol.* **37**, 668–679 (2016).
43. N. McDannold *et al*., Acoustic feedback enables safe and reliable carboplatin delivery across the blood-brain barrier with a clinical focused ultrasound system and improves survival in a rat glioma model. *Theranostics* **9**, 6284–6299 (2019).
44. N. D. Doolittle *et al*., Preservation of cognitive function in primary CNS lymphoma survivors a median of 12 years after enhanced chemotherapy delivery. *J. Clin. Oncol.* **31**, 4026–4027 (2013).
45. N. D. Doolittle *et al*., Safety and efficacy of a multicenter study using intraarterial chemotherapy in conjunction with osmotic opening of the blood-brain barrier for the treatment of patients with malignant brain tumors. *Cancer* **88**, 637–647 (2000).
46. J. A. Boockvar *et al*., Safety and maximum tolerated dose of superselective intraarterial cerebral infusion of bevacizumab after osmotic blood-brain barrier disruption for recurrent malignant glioma. Clinical article. *J. Neurosurg.* **114**, 624–632 (2011).
47. L. Angelov *et al*., Blood-brain barrier disruption and intra-arterial methotrexate-based therapy for newly diagnosed primary CNS lymphoma: A multi-institutional experience. *J. Clin. Oncol.* **27**, 3503–3509 (2009).
48. E. A. Neuwelt *et al*., Primary CNS lymphoma treated with osmotic blood-brain barrier disruption: Prolonged survival and preservation of cognitive function. *J. Clin. Oncol.* **9**, 1580–1590 (1991).
49. S. Chakraborty *et al*., Durability of single dose intra-arterial bevacizumab after blood/brain barrier disruption for recurrent glioblastoma. *J. Exp. Ther. Oncol.* **11**, 261–267 (2016).
50. S. A. Dahlborg *et al*., The potential for complete and durable response in nonglial primary brain tumors in children and young adults with enhanced chemotherapy delivery. *Cancer J. Sci. Am.* **4**, 110–124 (1998).
51. S. I. Rapoport, Osmotic opening of the blood-brain barrier: Principles, mechanism, and therapeutic applications. *Cell. Mol. Neurobiol.* **20**, 217–230 (2000).
52. R. Gabathuler, Approaches to transport therapeutic drugs across the blood-brain barrier to treat brain diseases. *Neurobiol. Dis.* **37**, 48–57 (2010).
53. L. A. Castro-Jorge *et al*., A protective role for interleukin-1 signaling during mouse adenovirus type 1-induced encephalitis. *J. Virol.* **91**, e02106-16 (2017).
54. D. Amantea *et al*., Understanding the multifaceted role of inflammatory mediators in ischemic stroke. *Curr. Med. Chem.* **21**, 2098–2117 (2014).
55. W. Jiang, W. J. Cao, Y. K. Zhang, X. Y. Wei, F. Kuang, Bolus injection of hypertonic solutions for cerebral edema in rats: Challenge of homeostasis of healthy brain. *Neurosci. Lett.* **509**, 44–49 (2012).
56. H. Al-Sarraf, F. Ghaaedi, Z. Redzic, Time course of hyperosmolar opening of the blood-brain and blood-CSF barriers in spontaneously hypertensive rats. *J. Vasc. Res.* **44**, 99–109 (2007).
57. L. L. Muldoon *et al*., A physiological barrier distal to the anatomic blood-brain barrier in a model of transvascular delivery. *AJNR Am. J. Neuroradiol.* **20**, 217–222 (1999).
58. T. S. Salahuddin, B. B. Johansson, H. Kalimo, Y. Olsson, Structural changes in the rat brain after carotid infusions of hyperosmolar solutions. An electron microscopic study. *Acta Neuropathol.* **77**, 5–13 (1988).
59. M. W. Lo, T. M. Woodruff, Complement: Bridging the innate and adaptive immune systems in sterile inflammation. *J. Leukoc. Biol.* **108**, 339–351 (2020).
60. M. A. Petersen, J. K. Ryu, K. Akassoglou, Fibrinogen in neurological diseases: Mechanisms, imaging and therapeutics. *Nat. Rev. Neurosci.* **19**, 283–301 (2018).
61. D. Shlosberg, M. Benifla, D. Kaufer, A. Friedman, Blood-brain barrier breakdown as a therapeutic target in traumatic brain injury. *Nat. Rev. Neurol.* **6**, 393–403 (2010).
62. F. Frigerio *et al*., Long-lasting pro-ictogenic effects induced in vivo by rat brain exposure to serum albumin in the absence of concomitant pathology. *Epilepsia* **53**, 1887–1897 (2012).
63. C. D. Savage, G. Lopez-Castejon, A. Denes, D. Brough, NLRP3-Inflammasome activating DAMPs stimulate an inflammatory response in glia in the absence of priming which contributes to brain inflammation after injury. *Front. Immunol.* **3**, 288 (2012).
64. H. Tokami *et al*.; REBIOS Investigators, RANTES has a potential to play a neuroprotective role in an autocrine/paracrine manner after ischemic stroke. *Brain Res.* **1517**, 122–132 (2013).
65. M. L. Kelso, B. R. Elliott, N. A. Haverland, R. L. Mosley, H. E. Gendelman, Granulocyte-macrophage colony stimulating factor exerts protective and immunomodulatory effects in cortical trauma. *J. Neuroimmunol.* **278**, 162–173 (2015).
66. K. Strle *et al*., Interleukin-10 in the brain. *Crit. Rev. Immunol.* **21**, 427–449 (2001).
67. H. H. Marti, Erythropoietin and the hypoxic brain. *J. Exp. Biol.* **207**, 3233–3242 (2004).
68. R. K. Stumm *et al*., A dual role for the SDF-1/CXCR4 chemokine receptor system in adult brain: Isoform-selective regulation of SDF-1 expression modulates CXCR4-dependent neuronal plasticity and cerebral leukocyte recruitment after focal ischemia. *J. Neurosci.* **22**, 5865–5878 (2002).
69. E. Kilic *et al*., The phosphatidylinositol-3 kinase/Akt pathway mediates VEGF's neuroprotective activity and induces blood brain barrier permeability after focal cerebral ischemia. *FASEB J.* **20**, 1185–1187 (2006).
70. J. E. Burda, A. M. Bernstein, M. V. Sofroniew, Astrocyte roles in traumatic brain injury. *Exp. Neurol.* **275**, 305–315 (2016).
71. M. V. Sofroniew, Astrocyte barriers to neurotoxic inflammation. *Nat. Rev. Neurosci.* **16**, 249–263 (2015).
72. M. Takamiya, S. Fujita, K. Saigusa, Y. Aoki, Simultaneous detections of 27 cytokines during cerebral wound healing by multiplexed bead-based immunoassay for wound age estimation. *J. Neurotrauma* **24**, 1833–1844 (2007).
73. D. Brough, A. Denes, Interleukin-1α and brain inflammation. *IUBMB Life* **67**, 323–330 (2015).
74. W. L. Thompson, L. J. Van Eldik, Inflammatory cytokines stimulate the chemokines CCL2/MCP-1 and CCL7/MCP-3 through NFkB and MAPK dependent pathways in rat astrocytes [corrected]. *Brain Res.* **1287**, 47–57 (2009).

75. M. Mao *et al*., MicroRNA-195 prevents hippocampal microglial/macrophage polarization towards the M1 phenotype induced by chronic brain hypoperfusion through regulating CX3CL1/CX3CR1 signaling. *J. Neuroinflammation* **17**, 244 (2020).
76. L. Vitkovic *et al*., Cytokine signals propagate through the brain. *Mol. Psychiatry* **5**, 604–615 (2000).
77. Q. Ma, B. V. Ineichen, M. Detmar, S. T. Proulx, Outflow of cerebrospinal fluid is predominantly through lymphatic vessels and is reduced in aged mice. *Nat. Commun.* **8**, 1434 (2017).
78. H. F. Cserr, Physiology of the choroid plexus. *Physiol. Rev.* **51**, 273–311 (1971).
79. Y. Meng *et al*., Glymphatics visualization after focused ultrasound-induced blood-brain barrier opening in humans. *Ann. Neurol.* **86**, 975–980 (2019).
80. J. J. Iliff *et al*., A paravascular pathway facilitates CSF flow through the brain parenchyma and the clearance of interstitial solutes, including amyloid β. *Sci. Transl. Med.* **4**, 147ra111 (2012).
81. I. C. M. Verheggen, M. P. J. Van Boxtel, F. R. J. Verhey, J. F. A. Jansen, W. H. Backes, Interaction between blood-brain barrier and glymphatic system in solute clearance. *Neurosci. Biobehav. Rev.* **90**, 26–33 (2018).
82. L. Cucullo *et al*., Blood-brain barrier damage induces release of alpha2-macroglobulin. *Mol. Cell. Proteomics* **2**, 234–241 (2003).
83. L. E. Pelinka *et al*., GFAP versus S100B in serum after traumatic brain injury: Relationship to brain damage and outcome. *J. Neurotrauma* **21**, 1553–1561 (2004).
84. H. J. Kim, J. W. Tsao, A. G. Stanfill, The current state of biomarkers of mild traumatic brain injury. *JCI Insight* **3**, e97105 (2018).
85. M. I. Bogorad, J. G. DeStefano, R. M. Linville, A. D. Wong, P. C. Searson, Cerebrovascular plasticity: Processes that lead to changes in the architecture of brain microvessels. *J. Cereb. Blood Flow Metab.* **39**, 1413–1432 (2019).
86. A. M. Malek, G. G. Goss, L. Jiang, S. Izumo, S. L. Alper, Mannitol at clinical concentrations activates multiple signaling pathways and induces apoptosis in endothelial cells. *Stroke* **29**, 2631–2640 (1998).
87. M. De Bock *et al*., Endothelial calcium dynamics, connexin channels and blood-brain barrier function. *Prog. Neurobiol.* **108**, 1–20 (2013).
88. C. T. Capaldo, A. Nusrat, Cytokine regulation of tight junctions. *Biochim. Biophys. Acta* **1788**, 864–871 (2009).
89. Y. Yao, S. E. Tsirka, Monocyte chemoattractant protein-1 and the blood-brain barrier. *Cell. Mol. Life Sci.* **71**, 683–697 (2014).
90. M. A. Lopez-Ramirez *et al*., Role of caspases in cytokine-induced barrier breakdown in human brain endothelial cells. *J. Immunol.* **189**, 3130–3139 (2012).
91. S. J. O'Carroll *et al*., Pro-inflammatory TNFα and IL-1β differentially regulate the inflammatory phenotype of brain microvascular endothelial cells. *J. Neuroinflammation* **12**, 131 (2015).
92. L. G. Remsen *et al*., The influence of anesthetic choice, PaCO2, and other factors on osmotic blood-brain barrier disruption in rats with brain tumor xenografts. *Anesth. Analg.* **88**, 559–567 (1999).
93. A. Burgess *et al*., Alzheimer disease in a mouse model: MR imaging-guided focused ultrasound targeted to the hippocampus opens the blood-brain barrier and improves pathologic abnormalities and behavior. *Radiology* **273**, 736–745 (2014).
94. A. Burgess, I. Aubert, K. Hynynen, Focused ultrasound: Crossing barriers to treat Alzheimer's disease. *Ther. Deliv.* **2**, 281–286 (2011).
95. T. Alecou, M. Giannakou, C. Damianou, Amyloid β plaque reduction with antibodies crossing the blood-brain barrier, which was opened in 3 sessions of focused ultrasound in a rabbit model. *J. Ultrasound Med.* **36**, 2257–2270 (2017).
96. G. Leinenga, J. Götz, Scanning ultrasound removes amyloid-β and restores memory in an Alzheimer's disease mouse model. *Sci. Transl. Med.* **7**, 278ra33 (2015).
97. Y. Meng *et al*., Focused ultrasound as a novel strategy for Alzheimer disease therapeutics. *Ann. Neurol.* **81**, 611–617 (2017).
98. R. M. Nisbet *et al*., Combined effects of scanning ultrasound and a tau-specific single chain antibody in a tau transgenic mouse model. *Brain* **140**, 1220–1230 (2017).
99. S. B. Raymond *et al*., Ultrasound enhanced delivery of molecular imaging and therapeutic agents in Alzheimer's disease mouse models. *PLoS One* **3**, e2175 (2008).
100. M. E. Karakatsani *et al*., Unilateral focused ultrasound-induced blood-brain barrier opening reduces phosphorylated tau from the rTg4510 mouse model. *Theranostics* **9**, 5396–5411 (2019).
101. C. T. Poon *et al*., Time course of focused ultrasound effects on β-amyloid plaque pathology in the TgCRND8 mouse model of Alzheimer's disease. *Sci. Rep.* **8**, 14061 (2018).
102. A. Burgess, T. Nhan, C. Moffatt, A. L. Klibanov, K. Hynynen, Analysis of focused ultrasound-induced blood-brain barrier permeability in a mouse model of Alzheimer's disease using two-photon microscopy. *J. Control. Release* **192**, 243–248 (2014).
103. M. A. O'Reilly *et al*., Investigation of the safety of focused ultrasound-induced blood-brain barrier opening in a natural canine model of aging. *Theranostics* **7**, 3573–3584 (2017).
104. N. Nagarsheth, M. S. Wicha, W. Zou, Chemokines in the cancer microenvironment and their relevance in cancer immunotherapy. *Nat. Rev. Immunol.* **17**, 559–572 (2017).
105. J. Adhikaree, J. Moreno-Vicente, A. P. Kaur, A. M. Jackson, P. M. Patel, Resistance mechanisms and barriers to successful immunotherapy for treating glioblastoma. *Cells* **9**, 263 (2020).
106. D. Kwok, H. Okada, T-Cell based therapies for overcoming neuroanatomical and immunosuppressive challenges within the glioma microenvironment. *J. Neurooncol.* **147**, 281–295 (2020).
107. J. Galon, D. Bruni, Approaches to treat immune hot, altered and cold tumours with combination immunotherapies. *Nat. Rev. Drug Discov.* **18**, 197–218 (2019).
108. J. Galon *et al*., Type, density, and location of immune cells within human colorectal tumors predict clinical outcome. *Science* **313**, 1960–1964 (2006).
109. S. Taheri, C. Gasparovic, N. J. Shah, G. A. Rosenberg, Quantitative measurement of blood-brain barrier permeability in human using dynamic contrast-enhanced MRI with fast T1 mapping. *Magn. Reson. Med.* **65**, 1036–1042 (2011).
110. W. Y. Huang *et al*., Multi-parameters of magnetic resonance imaging to estimate ischemia-reperfusion injury after stroke in hyperglycemic rats. *Sci. Rep.* **9**, 2852 (2019).
111. J. Naidoo, H. Panday, S. Jackson, S. A. Grossman, Optimizing the delivery of antineoplastic therapies to the central nervous system. *Oncology (Williston Park)* **30**, 953–962 (2016).
112. R. A. Kroll *et al*., Improving drug delivery to intracerebral tumor and surrounding brain in a rodent model: A comparison of osmotic versus bradykinin modification of the blood-brain and/or blood-tumor barriers. *Neurosurgery* **43**, 879–886 (1998).
113. S. Lê, J. Josse, F. Husson, FactoMineR: An R package for multivariate analysis. *J. Stat. Software* **25**, 18 (2008).
114. A. Subramanian *et al*., Gene set enrichment analysis: A knowledge-based approach for interpreting genome-wide expression profiles. *Proc. Natl. Acad. Sci. U.S.A.* **102**, 15545–15550 (2005).
115. A. Liberzon *et al*., Molecular signatures database (MSigDB) 3.0. *Bioinformatics* **27**, 1739–1740 (2011).
116. A. Liberzon *et al*., The Molecular Signatures Database (MSigDB) hallmark gene set collection. *Cell Syst.* **1**, 417–425 (2015).
117. D. Merico, R. Isserlin, O. Stueker, A. Emili, G. D. Bader, Enrichment map: A network-based method for gene-set enrichment visualization and interpretation. *PLoS One* **5**, e13984 (2010).